inorganics

MDPI

Article

Structural Control and Electrical Behavior of Thermally Reduced Graphene Oxide Samples Assisted with Malonic Acid and Phosphorus Pentoxide

Ruta Aukstakojyte [1], Justina Gaidukevic [1,*], Gediminas Niaura [2], Martynas Skapas [3], Virginijus Bukauskas [4] and Jurgis Barkauskas [1]

[1] Faculty of Chemistry and Geosciences, Vilnius University, Naugarduko Str. 24, LT-03225 Vilnius, Lithuania
[2] Department of Organic Chemistry, Center for Physical Sciences and Technology, Saulėtekio Ave. 3, LT-10257 Vilnius, Lithuania
[3] Department of Characterisation of Materials Structure, Center for Physical Sciences and Technology, Saulėtekio Ave. 3, LT-10257 Vilnius, Lithuania
[4] Department of Physical Technologies, Center for Physical Sciences and Technology, Saulėtekio Ave. 3, LT-10257 Vilnius, Lithuania
* Correspondence: justina.gaidukevic@chf.vu.lt

Abstract: We present a detailed study of the structural and electrical changes occurring in two graphene oxide (GO) samples during thermal reduction in the presence of malonic acid (MA) (5 and 10 wt%) and P_2O_5 additives. The morphology and de-oxidation efficiency of reduced GO (rGO) samples are characterized by Fourier transform infrared, X-ray photoelectron, energy-dispersive X-ray, Raman spectroscopies, transmission electron and scanning electron microscopies, X-ray diffraction (XRD), and electrical conductivity measurements. Results show that MA and P_2O_5 additives are responsible for the recovery of π-conjugation in rGO as the XRD pattern presents peaks corresponding to (002) graphitic-lattice planes, suggesting the formation of the sp^2-like carbon structure. Raman spectra show disorders in graphene sheets. Elemental analysis shows that the proposed reduction method in the presence of additives also suggests the simultaneous insertion of phosphorus with a relatively high content (0.3–2.3 at%) in rGO. Electrical conductivity measurements show that higher amounts of additives used in the GO reduction more effectively improve electron mobility in rGO samples, as they possess the highest electrical conductivity. Moreover, the relatively high conductivity at low bulk density indicates that prepared rGO samples could be applied as metal-free and non-expensive carbon-based electrodes for supercapacitors and (bio)sensors.

Keywords: thermally reduced graphene oxide; carbon suboxide; phosphorus doped reduced graphene oxide; structural analysis; electrical conductivity

Citation: Aukstakojyte, R.; Gaidukevic, J.; Niaura, G.; Skapas, M.; Bukauskas, V.; Barkauskas, J. Structural Control and Electrical Behavior of Thermally Reduced Graphene Oxide Samples Assisted with Malonic Acid and Phosphorus Pentoxide. *Inorganics* **2022**, *10*, 142. https://doi.org/10.3390/inorganics10090142

Academic Editor: Hiroshi Kageyama

Received: 29 August 2022
Accepted: 13 September 2022
Published: 16 September 2022

1. Introduction

Reduced graphene oxide (rGO) possesses properties between graphene oxide (GO) and graphene that makes it an attractive carbon material in the applications of energy storage systems, (bio)sensors, fuel cells, Li^+ ion batteries, supercapacitors, etc. [1–3]. Several synthesis strategies of rGO have been proposed, which could be mainly categorized into the chemical, electrochemical, and thermal reduction of GO. Chemical reduction is a fast and straightforward method to obtain rGO at low temperatures (below 90 °C). However, reducing agents (hydrazine, lithium aluminum hydride, hydroiodic acid) used are harmful and highly toxic [3,4]. Moreover, the complete removal of reductants is complicated due to their adsorption on the rGO lattice [5]. Electrochemical reduction of GO is considered a green synthesis approach, but it is not cost-effective in terms of large-scale production of rGO. As a scalable, eco-friendly, rapid, and inexpensive method, thermal reduction is more attractive than chemical and electrochemical treatments. The thermally reduced GO

exhibits a higher reduction degree, larger specific surface area as well as better electronic properties compared to rGO samples prepared by the chemical process. Furthermore, thermal reduction is a promising method for the industrial preparation of rGO with less damage to the environment [3].

However, the thermal reduction of GO is still challenging. Annealing of GO leads to high volumes of CO and CO_2 gases that cause structural disorders such as Stone–Wales defects, C vacancies, dislocations, grain boundaries, and sp^3 defects [6]. It is well known that these disorders alter the length of C–C bonds and induce the σ and π orbitals re-hybridization. They may cause the scattering of electron waves and the change of electrons trajectories resulting in a decrease of electron carrier mobility and electrical conductivity in the sample. The presence of distortions can also deteriorate physical properties such as the thermal conductivity and mechanical strength of the material [7]. For these reasons, it is essential to focus on the synthesis procedure to ensure the best recovery of the sp^2 carbon network in the rGO.

The final properties of rGO, including the C/O ratio, number of layers, surface area, and number of structural defects, could be controlled by changing thermal reduction conditions such as temperature, pressure, atmosphere, and oxidation degree of GO. The study reported by A. Kaniyoor et al. showed that the use of the H_2 and Ar mixture in the synthesis of rGO leads to a higher C/O ratio compared to that of the sample reduced only under Ar atmosphere [8]. Then, at higher temperatures (1000–2800 °C), the restoration of the sp^2 carbon network occurs more effectively than at lower temperatures due to the more pronounced decomposition of oxygen-containing functional groups and stimulation of graphitization [9,10]. The higher oxidation degree of GO influences the more efficient reduction process [11]. The substantial carbon source in thermal reduction of GO can also improve the restoration of the π-conjugated system, make a beneficial change in electrical properties, and decrease structural defects. For instance, Y. Liang et al. carried out thermal GO reduction in the presence of acetylene (C_2H_2) at 1000 °C temperature in order to prepare transparent graphene-based coatings for electrode materials. The sample obtained exhibited electrical conductivity more than four times higher than the compound in the absence of C_2H_2, representing the significant advantage of using additional carbon [12]. Following this, carbon suboxide (C_3O_2) may also be a good candidate as an atomic carbon source in the thermal reduction of GO. Formally, C_3O_2 is an anhydride of malonic acid ($CH_2(COOH)_2$); therefore, this carbon oxide could be produced by dehydration of malonic acid (MA) and a strong dehydrating agent, phosphorus pentoxide (P_2O_5), at 150 °C temperature [13]. C_3O_2 is gaseous and thermally decomposes into elemental carbon and two carbon monoxide molecules above 16 °C [14]. For this reason, this linear molecule has been successfully used as an atomic carbon source in the synthesis of carbon nanotubes and carbon coatings [15,16]. Additionally, our previous study showed the positive impact of C_3O_2 on the decomposition kinetics of GO and the structural properties of rGO obtained at relatively low temperatures (250 °C) [17]. Surprisingly, the use of the MA and P_2O_5 mixture could be beneficial in the thermal reduction of GO since the reaction between these two compounds produces C_3O_2 as well as H_3PO_4. According to the literature, phosphorus acid has been used as an effective dopant of phosphorus atoms in the chemical and thermal reduction of GO [18–21]. Modification with phosphorus can effectively modulate the electrical, catalytic, and electrochemical properties of rGO. The phosphorus atom has lower electronegativity than the carbon atom that changes charge densities in the graphene-based material resulting in enhanced capacitive performance and surface area of phosphorus-doped graphene compounds [21–23]. Moreover, the incorporation of phosphorus atoms increases the density of charge carries in the carbon sample due to the contribution of phosphorus electrons to the π-conjugated system of rGO. For this reason, the electrical conductivity is expected to increase [24]. Thus, we propose that this suggested thermal reduction technique with an additive of MA and P_2O_5 will provide new possibilities to achieve materials with restored sp^2 carbon network and improved electrochemical performance to successfully apply new phosphorus-doped rGO materials in (bio)sensors or supercapacitors. To the

best of our knowledge, the mixture of MA and P_2O_5 has been used for the first time as a reducing mixture and phosphorus-containing agent for the reduction and modification of GO. Moreover, the detailed structural characterization and electrical conductivity behavior of rGO obtained using the mixture of MA and P_2O_5 have not been investigated in depth yet.

The aim of this research was to evaluate the changes in the structure and electrical behavior of different rGO samples prepared using thermal reduction of GO in the absence and presence of MA and P_2O_5 mixture. Two GO samples with different oxidation degrees and functional groups were used to prepare rGO samples. We have demonstrated the enhanced successful restoration of the π-conjugated system, as well as the simultaneous incorporation of phosphorus atoms. The impact of C_3O_2 and the insertion of phosphorus atoms on structural properties and morphology was evaluated in detail using X-ray diffraction (XRD), energy dispersive X-ray spectroscopy (EDX), X-ray photoelectron spectroscopy (XPS), Fourier transform infrared spectroscopy (FTIR), scanning electron microscopy (SEM), transmission electron microscopy (TEM), and Raman spectroscopies. Electrical conductivity measurements of synthesized rGO samples with additives were also carried out.

2. Materials and Methods

2.1. Preparation of GO Samples

2.1.1. GO Synthesis Using Pre-Oxidation with $K_2S_2O_8$, P_2O_5, and H_2SO_4 Mixture

Pretreatment of graphite was performed by the synthesis protocol described in the work of Yan et al. [25]. In a typical experiment, natural graphite powder (6.0 g) was mixed with $K_2S_2O_8$ (5.0 g) and P_2O_5 (5.0 g) in the 98 wt% H_2SO_4 (24.0 mL) media. Subsequently, this pre-oxidized graphite obtained was subjected to oxidation, following the protocol reported by Hummers et al. [26]. The GO suspension formed in the reaction was transferred into a dialysis tubing cellulose membrane with a cut-off molecular weight of 10,000–20,000 Da for further purification and dialyzed against distilled water until the pH value of the dialysate became ~5. The brown powder obtained was dried in air at ambient temperature to a constant weight. The prepared powder sample was denoted as GO_1.

2.1.2. GO Synthesis Using Pre-Oxidation with H_2SO_4, H_3BO_3, and CrO_3 Mixture

In this study, pre-oxidation of graphite was carried out according to the new approach proposed in our laboratory [27]. In this method, graphite powder (2.0 g) was added to the mixture of 98 wt% H_2SO_4 (11.0 mL) and H_3BO_3 (0.78 g) with steady and vigorous stirring. Later, CrO_3 (2.1 g) was gradually added and the reaction mixture was maintained for 2 h at 45−55 °C. Afterwards, the resulting suspension was washed with warm distilled H_2O to remove the excess H_3BO_3. Further oxidation of this pre-oxidized graphite was performed using Hummers' method [26]. The GO suspension was purified by dialysis as previously described and dried in air to a constant weight. The product obtained was named as GO_2.

2.2. Thermal Reduction of GO Samples

Each synthesized GO sample (GO_1 and GO_2) mixed with MA and phosphorus pentoxide was ground in an agate mortar for 10 min. The weight ratios of GO and MA used in this mechanochemical synthesis were 1:0.05 and 1:0.10. The amount of phosphorus pentoxide was calculated according to the following equation:

$$3C_3H_4O_4 + P_4O_{10} \rightarrow 3C_3O_2 + 4H_3PO_4 \quad (1)$$

The solid mixtures prepared after grinding were reduced in the tubular furnace exposing them at 100 °C for 10 min. Later, the samples obtained were treated by thermal shock at 800 °C for 5 min. The whole heat treatment process (at 100 °C and 800 °C temperatures) was carried out under an argon atmosphere with a flow rate of 60 mL/min. After cooling, the thermally reduced GO samples were thoroughly washed with deionized water and dried in air. The thermal reduction of the GO samples without additives was also performed under the same synthesis conditions. The samples obtained were labelled

rGO_1 and rGO_2, respectively. Whereas, thermally reduced GO_1 and GO_2 samples with the addition of MA and phosphorus pentoxide were named according to the ratio of added MA. For example, if GO_1 was thermally reduced by adding 5 wt% or 10 wt% of MA, this synthesized product was denoted as rGO_1_5 or rGO_1_10, respectively.

2.3. Material Characterization

The crystallographic information of the synthesized products was obtained using a MiniFlex II X-ray diffractometer (Rigaku, Tokyo, Japan). XRD patterns were recorded in the 2θ range from 5° to 60° using CuKα λ = 1.5406 Å radiation with a step of 0.010°. The interlayer distance d of the prepared samples was evaluated using Bragg's equation:

$$n\lambda = 2dsin\theta \quad (2)$$

where λ is the wavelength of the X-ray beam, n is a positive integer, d is the interlayer distance, and θ is the diffraction angle. The average crystallite size D was calculated by determining the full-width at the half-maximum (FWHM) of the diffraction peaks using the Debye–Scherrer's equation as follows:

$$D = \frac{K\lambda}{\beta cos\theta} \quad (3)$$

where K is a constant (0.89), λ is the wavelength of the X-ray radiation, β is the FWHM of the peak, and θ is the diffraction angle. D for the graphite and rGO samples was determined from the (002) planes, while D for the GO samples was calculated from the (001) planes.

EDX analysis was performed by a scanning electron microscope (TM3000; Hitachi, Tokyo, Japan) equipped with an EDX detector.

XPS analysis was carried out with a Kratos Axis Supra (Kratos analytical, Manchester, UK) spectrometer. Monochromatic Al Kα radiation ($h\nu$ = 1486.69 eV) was used as an X-ray source. The XPS P2p spectrum was recorded at a pass energy of 20 eV and calibrated using the carbon 1 s line at 284.6 eV. The raw XPS spectrum was deconvoluted by curve fitting peak components using the software CASAXPS. Symmetric Gaussian–Lorentzian functions were used to approximate the line shapes of the fitting components after the Shirley-type background subtraction.

FTIR spectroscopy measurements were performed by an FTIR spectrometer (PerkinElmer, Inc., Waltham, MA, USA). Infrared spectra were recorded in the range of 700–4000 cm^{-1} using the KBr pellet technique in transmission mode. The spectral resolution was set at 4 cm^{-1}.

Raman spectra were recorded using an inVia Raman spectrometer (Renishaw, Wotton-under-Edge, UK) equipped with a thermoelectrically cooled (−70 °C) CCD camera in the range of 300–3300 cm^{-1}. The He-Ne gas laser provided an excitation beam at 532 nm with power restricted to 1 mW. The integration time was selected as 100 s. The average in-plane crystallite size $L\alpha$ was determined according to the following equation [28]:

$$L\alpha = 2.4 \times 10^{-10} \times \lambda_L^4 \times \left[\frac{I_D}{I_G}\right]^{-1} \quad (4)$$

where λ_L is the wavelength of the laser radiation used for the excitation of the Raman analysis, and I_D and I_G are the intensities of the D and G bands in the Raman spectra, respectively.

SEM imaging was carried out using a Hitachi SU-70 microscope at an accelerating voltage of 10.0 kV at magnifications of 50,000. The samples were coated with 10 nm of silver using a Q150T ES Turbo-Pumped Sputter Coater (Quorum, Washington, DC, USA) before SEM microscopy.

TEM analysis was performed using a TECNAI G2 F20 X-TWIN microscope equipped with an Orius SC1000B CCD camera (Gatan, Pleasanton, CA, USA) with a Schottky-type field emission electron source using an accelerating voltage of 200 kV. Selected area electron

diffraction (SAED) patterns on thermally reduced samples transferred on copper mesh were recorded using the SAED diaphragm.

A Keithley 2601 Source Meter (GlobalTech Sourcing, North Hampton, NH, USA) was applied for the conductivity measurement. The electrical conductivity of the rGO samples obtained was determined using a cell made in our laboratory. The experiments were carried out at room temperature (22 °C) and a relative humidity of 40%. Approximately 0.02 g of rGO powder samples were placed in a glass cylinder of 2.86 mm in diameter between two copper electrodes. We assume that the electrical contact area between the electrode and the powder was the same as the inner area of a cylinder. The sample was gradually pressed by reducing the distance between the electrodes, and the resistance was determined. The resistivity (ρ) was determined using the following equation:

$$\rho = R\frac{A}{l} \quad (5)$$

where, R is a resistance (Ω), A is a cross section area (m^2), and l is length of the sample (m). It is important to note that current-voltage characteristic curves were linear in a voltage range of ± 1 V for all tested samples.

3. Results and Discussion

The elemental composition of the synthesized GO and rGO samples is presented in Figure 1a,b. As can be seen in Figure 1a,b, GO_1 and GO_2 contain carbon, oxygen, and sulfur atoms. The origin of sulfur is associated with the presence of HSO_4^- and SO_4^{2-} residuals, introduced during the oxidation treatment of pristine graphite. Moreover, the C/O ratio of GO_2 is determined to be 1.66 indicating the higher oxidation degree compared to that of GO_1 (C/O = 1.95). After thermal treatment of GO samples without MA and P_2O_5 additives, only carbon and oxygen elements are identified for rGO_1 and rGO_2 and the ratio of C/O significantly increased up to 11.66 and 8.68 for rGO_1 and rGO_2, respectively. Besides, from Figure 1a,b, it can be noted that the relative concentration of oxygen has been reduced from 33.6 at% and 37.4 at% for GO_1 and GO_2, respectively, to 7.9 at% for rGO_1 and 9.6 at% for rGO_2, suggesting a partial reduction of the GO samples. On the contrary, the samples obtained after thermal reduction of GO using a mixture of MA and P_2O_5 consist of carbon, oxygen, and phosphorus atoms. The similar tendency of the increasing of C/O values is observed for all rGO samples obtained using additives in the reduction process. The determined C/O values for rGO_1_5, rGO_1_10, rGO_2_5, and rGO_2_10 are 8.68, 7.02, 7.71, and 6.24, respectively. Supposedly, phosphorus functionalities enter the structure of rGO samples due to the formation of H_3PO_4 in the reaction between MA and P_2O_5 (Equation (1)). As can be seen in Figure 1a,b, the content of phosphorus varies from 0.3 to 2.3 at%, while the highest content of P (2.3 at%) is determined in the rGO_2_10 sample. It should be noted that the phosphorus-doping level in this sample is much higher than other previously synthesized phosphorus-doped rGO samples reported in the literature [18,19,29,30]. Furthermore, the results obtained from the elemental analysis show that the amount of oxygen increases with an increase of the additives content used in the thermal reduction process. In the case of rGO_1 samples, the oxygen contents are 10.3 at% and 12.3 at% for rGO_1_5 and rGO_1_10, respectively, while in the case of rGO_2 samples, the oxygen contents are 11.4 at% and 13.5 at% for rGO_2_5 and rGO_2_10 samples, respectively. It could be a consequence of introducing oxygen-containing phosphate groups (O–P or O=P) into the graphene structure. The P2p XPS spectrum could provide detailed information on the phosphorus-containing functional groups presented on the surface of samples. As only two samples, rGO_1_10 and rGO_2_10, exhibited a higher amount of phosphorus, they were selected for a P2p peak deconvolution analysis, and the results are presented in Figure 1c,d. It can be noted that for both samples, deconvolution of the P2p region presents an inseparable doublet with $P2p_{1/2}$ and $P2p_{3/2}$ components at ΔBE = 0.8 eV and an area ratio of 1:2. A low energy doublet with the energy of the $P2p_{3/2}$ component of 132.6 eV is assigned to the C–P=O bonds. An intense doublet with the $P2p_{3/2}$ component located

at approximately 133.8 eV corresponds to the higher oxidation state of phosphorus [31]. Regarding the content of specific phosphorus-containing functionalities in the samples, it can be noticed that the reduction of GO in the presence of the MA and P_2O_5 additive leads to the formation of mainly the higher oxidation state of phosphorus (PO_x), as the relative concentration of these groups in the rGO_2_10 sample is 74.9 at% and in the case of the rGO_1_10 sample is 81.4 at%. The content of the C–P=O groups was considerably lower (25.1 at% for rGO_2_10 and 18.6 at% for rGO_1_10). Overall, these results confirm the partial reduction of GO samples and present a new kind of dopant for the successful insertion of phosphorus functionalities in the thermally reduced GO structure.

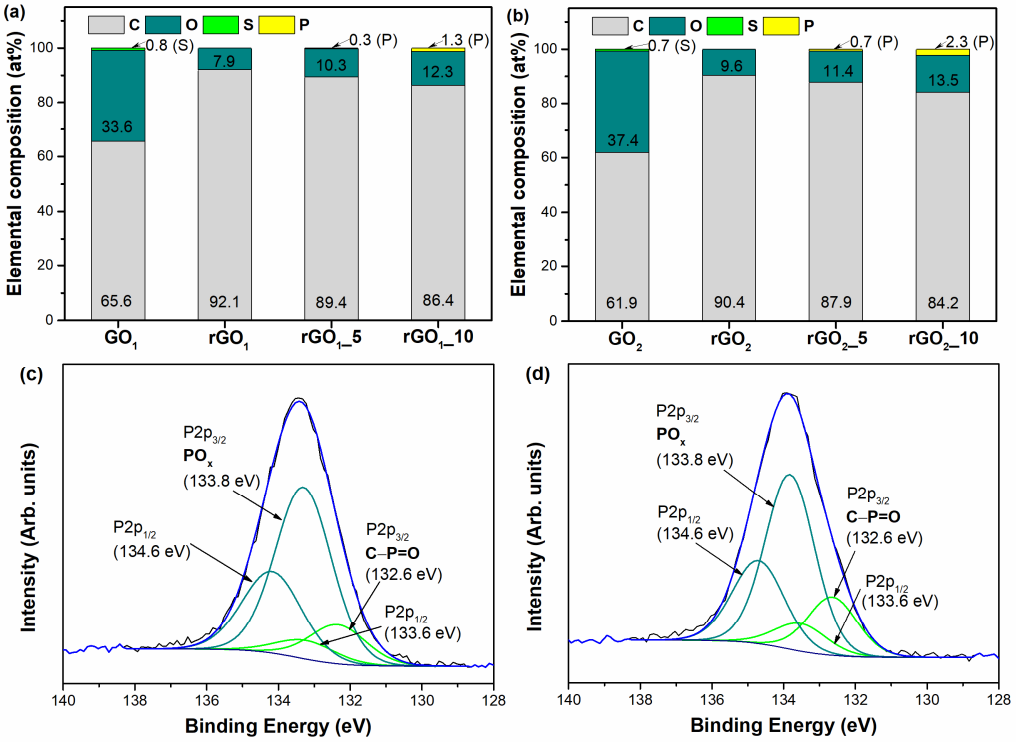

Figure 1. Elemental composition of GO_1 and thermally reduced samples derived from GO_1 (**a**), GO_2 and thermally reduced samples derived from GO_2 (**b**) based on EDX results. The P2p XPS spectra of rGO_1_10 (**c**) and rGO_2_10 (**d**) samples.

The functional groups on the surface of the samples obtained have been identified by FTIR spectroscopy. Figure 2 demonstrates the FTIR spectra of the graphite, GO_1, GO_2, and rGO samples. In the spectrum of pristine graphite (Figure 2a), the non-intensive absorption bands located at 2924 and 2853 cm^{-1} correspond to the symmetric and asymmetric stretching modes of the C–H bonds [32]. Then, a peak at 3444 cm^{-1} is attributed to the –OH bonds of adsorbed water molecules. The band at 1633 cm^{-1} arises due to the vibrations of aromatic C=C bonds, while the peaks at 1420 and 1052 cm^{-1} are ascribed to the vibrations of the phenolic (C–OH) and epoxy groups (C–O), respectively [33,34]. The FTIR spectra of the GO_1 and GO_2 samples (Figure 2a) exhibit quite a similar shape, which may reflect the similar surface composition of these materials. The width and intense band at 3444 cm^{-1} corresponds to –OH stretching vibration [35]. The new peak appearing at 1730 cm^{-1} could be attributed to C=O stretching vibrations in carboxyl or carbonyl groups, while the presence of the band at 1622 cm^{-1} could be related to the stretching of C=C bonds from unoxidized sp^2 carbon domains or C=O bonds in quinone groups [34]. The band centered at 1420 cm^{-1} is ascribed to –OH deformation vibrations of tertiary C–OH. The absorption modes at 1280 cm^{-1} and 1222 cm^{-1} are assigned to the C–O–C stretching vibrations in the epoxy functional group [33]. Moreover, two quite intense methylene group stretching bands at 2924 and 2853 cm^{-1} are identified in the spectrum of GO_2, indicating the presence

of sp^3 hybridized carbon regions [32]. Furthermore, the new absorption band centered at 800 cm^{-1} could be attributed to the deformation vibrations of C–H bonds of aromatic rings [33]. The above results demonstrate the presence of hydroxyl, carboxyl, quinone, and epoxy-functional groups and aromatic domains in the structure of GO samples, consistent with results reported elsewhere [34,36]. Most of these peaks are also present in the rGO_1 and rGO_2 samples (Figure 2b,c), but with significantly lower intensities. This notable decrease in the intensity confirms the partial decomposition of oxygen-containing functional groups during the thermal reduction of GO_1 and GO_2 samples. The non-intensive vibrational bands at 3440 cm^{-1} and in the range of 1730–950 cm^{-1} indicate the remaining hydroxyl, carbonyl, quinone, epoxy, and phenolic functional groups after annealing of GO samples.

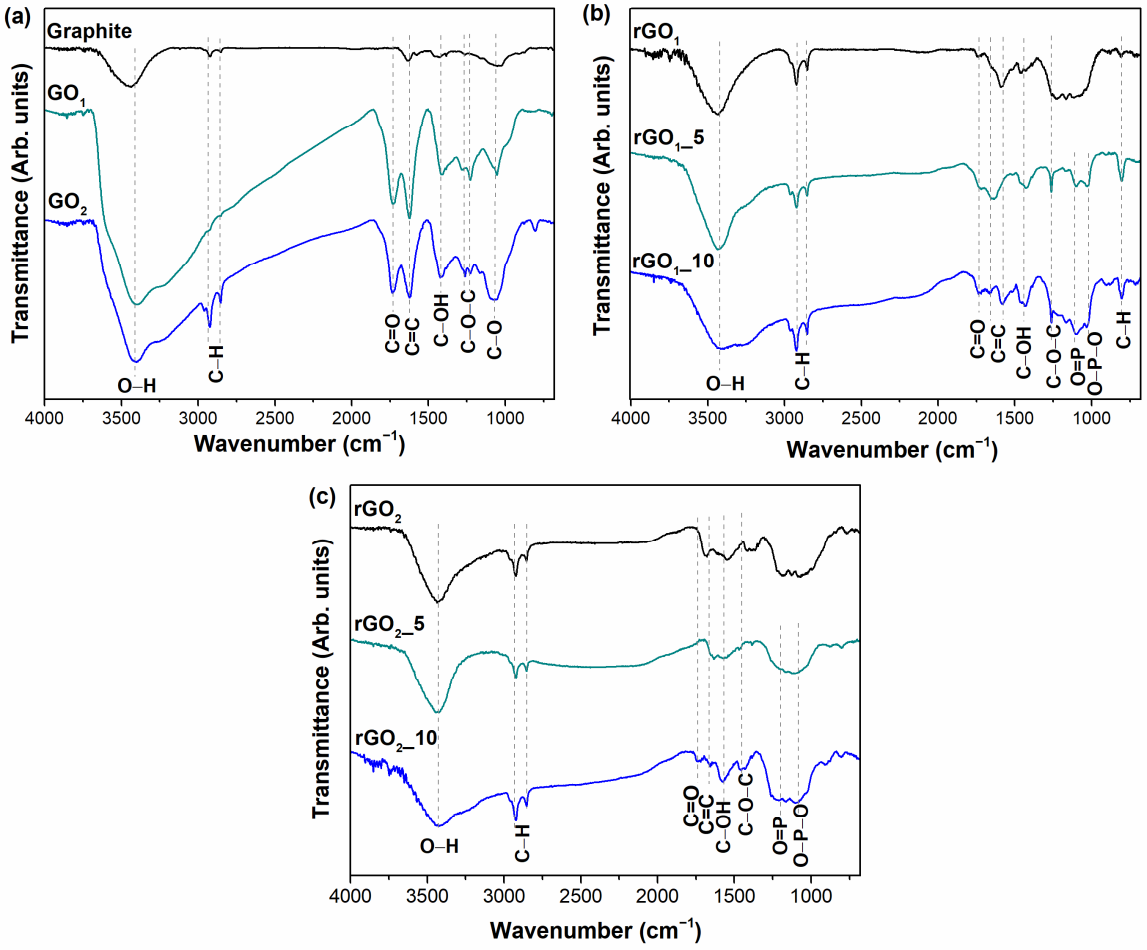

Figure 2. FTIR spectra of graphite, GO_1, and GO_2 (**a**); thermally reduced samples derived from GO_1 (**b**); and thermally reduced samples derived from GO_2 (**c**).

The thermal reduction of GO_1 with the mixture of MA (5 and 10 wt%) and P_2O_5 leads to the formation of the same functional groups as can be seen in the FTIR spectrum of rGO_1 (Figure 2b). Nevertheless, the new peaks appear at 1260, 1160, 1104, and 802 cm^{-1} that could be attributed to the formation of C–O–C, O=P, O–P–O, and C–H bonds on the surface of rGO_1_5 and rGO_1_10 samples, respectively [33,37]. The presence of phosphorus-containing bonds in those samples confirms the assumption of successful incorporation of P species into the structure of graphene. After thermal treatment of GO_2 with MA and P_2O additive, the FTIR spectra of the rGO_2_5 and rGO_2_10 samples (Figure 2c) exhibit quite similar spectra, which may reflect similar surface composition of these materials. The spectra of rGO_2_5 and rGO_2_10 contain a peak at 3440 cm^{-1} characterizing the vibrations of –OH bonds and bands at 2924 and 2853 cm^{-1} identifying the presence of C–H bonds [34]. However, the FTIR spectrum of rGO_2_5 exhibits two broad absorption bands in the ranges

of 1680–1440 cm^{-1} and 1310–950 cm^{-1}. The first wide band can be assigned to the stretching of the C=O and C=C bonds, while the second broad band may present the vibration of the C–O–C, C–OH, O=P, and O–P–O bonds [33,37]. The broad band in the range of 1310–950 cm^{-1} is also observed in the spectrum of the rGO_2_10 sample that indicates the phosphorus insertion in this sample [37]. Furthermore, the absorption band at 1580 cm^{-1} is related to C=C bonds from aromatic domains showing the partially restored sp^2 hybridized carbon structure in rGO_2_10. These data confirm the results of the XPS measurement showing the effective functionalization of rGO with phosphorus-containing functional groups.

The structural changes of the synthesized samples have been investigated by XRD analysis. The XRD patterns of the graphite, GO, and rGO samples are presented in Figure 3.

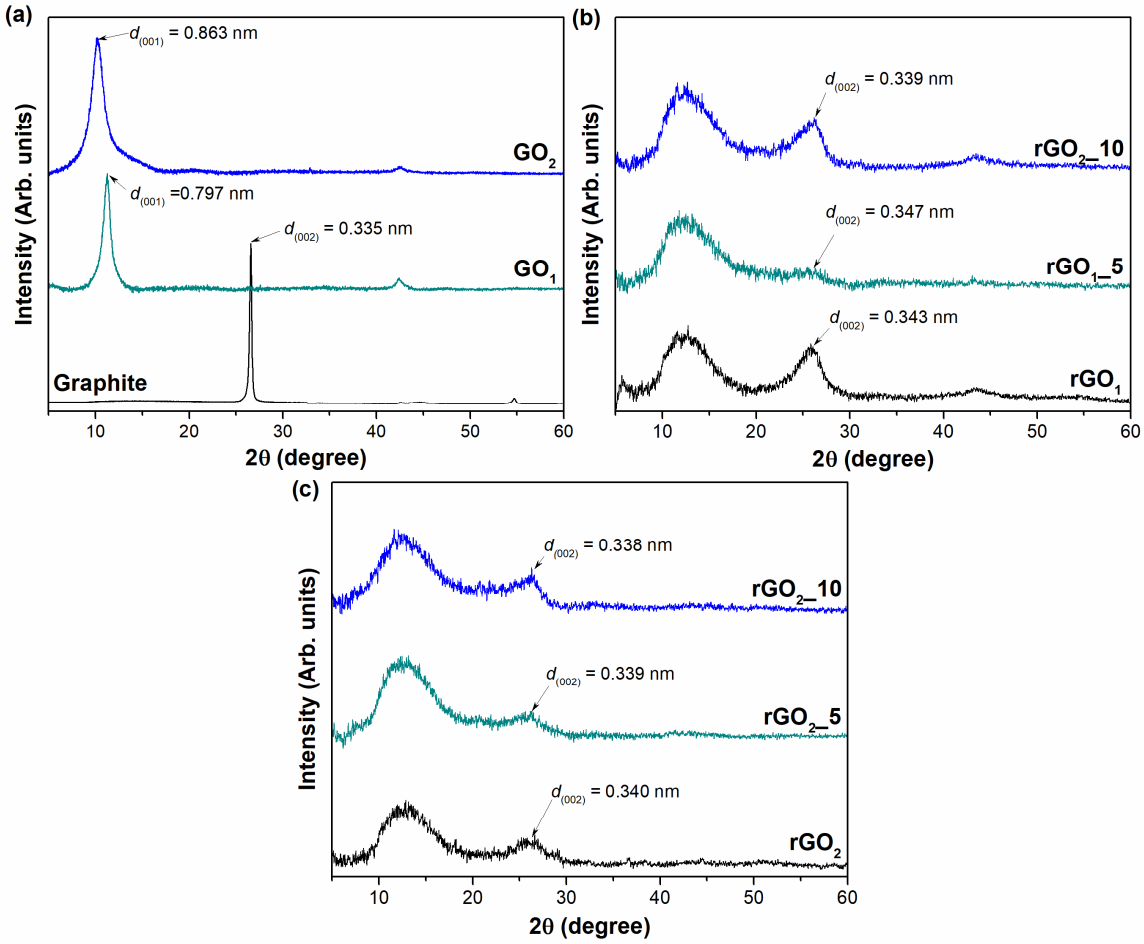

Figure 3. XRD patterns of graphite and synthesized GO samples (**a**), thermally reduced samples derived from GO_1 (**b**), and thermally reduced samples derived from GO_2 (**c**).

The XRD pattern of the pristine graphite powder (Figure 3a) exhibits a characteristic peak at 2θ = 26.60° corresponding to the (002) diffraction reflection and a low-intensity peak at 2θ = 54.70° that is related to the (004) plane of the hexagonal lattice. According to Bragg's equation, the interlayer distance $d_{(002)}$ is determined to be 0.335 nm, which is a typical d-spacing value of graphite. The crystallite size D reaches a value of about 31.98 nm. After the oxidation process, the (002) reflection disappears, while two new peaks arise in the ranges of 2θ = 10–11.5° (001) and at 2θ = 42.38° (100) in both cases of GO_1 and GO_2. The peaks of the (001) planes shift to lower 2θ angles of 11.28° and 10.24° for the GO_1 and GO_2 samples compared to that of graphite, respectively, due to intercalation of water and the attachment of oxygen-containing functional groups onto the graphitic carbon lattice. Moreover, this results in an increase of the interlayer distance from 0.335 nm in the case of graphite to 0.797 nm and 0.863 nm for the GO_1 and GO_2 samples, respectively. These

values are in good agreement with previous reports found in the literature [38,39]. The more significant expansion of the d-spacing for the GO_2 sample in comparison with that of GO_1 reveals that the higher oxidation degree of GO is achieved using a pre-oxidation step with the mixture of H_2SO_4, H_3BO_3, and CrO_3. The values of the crystallite size are estimated to be 8.41 nm and 4.50 nm for the GO_1 and GO_2 samples, respectively. It suggests that smaller crystallites are obtained during the synthesis of GO_2 because of the more substantial interruption of the structure due to the higher amount of oxygen-containing functional groups on the GO_2 surface.

Figure 3b,c presents the XRD results of thermally reduced GO_1 and GO_2 samples obtained with and without the use of MA and P_2O_5 additive, respectively. After annealing of GO_1, significant structural differences and changes in crystallinity are observed in all analyzed samples (Figure 3b). The XRD patterns of the samples produced become broader because of the breakdown of the long-range structure of the GO. Notably, a characteristic diffraction peak of GO (001) still remains in the XRD pattern of the rGO_1 samples (at approximately 2θ = 12.68–12.80°) and corresponds to interlayer spacing distances of 0.705 nm, 0.702 nm, and 0.692 nm for rGO_1, rGO_1_5, and rGO_1_10, respectively. This can support the conclusion of the elemental analysis, indicating that the reduction of graphene oxide to rGO is incomplete and that residual oxygen-containing functional groups are still present on the surface of rGO_1. It is important to note that the existence of the (001) plane in the rGO_1 samples may suggest the presence of thermally stable (at least at 800 °C) oxygen-containing functionalities, such as carbonyl, quinone, or pyrone groups, in the structure of the rGO samples. On the contrary, it is possible that the fraction of less stable functionalities may remain in the samples since the thermal shock time was relatively short. This could explain the reasons why rGO_1 samples are still high in oxygen [40]. Nevertheless, a characteristic (002) peak of graphite was observed at 2θ = 25.92° for the rGO_1, 2θ = 25.63° for the rGO_1_5, and 2θ = 26.23° for the rGO_1_10 samples, yielding an interlayer separation of 0.343 nm, 0.347 nm, and 0.339 nm for rGO_1, rGO_1_5, and rGO_1_10, respectively. This indicates that GO_1 reduction has occurred.

The XRD data of the annealed GO_2 samples with and without additives are presented in Figure 3c. The same trend is noticed that after the thermal reduction of GO_2, the peaks in the XRD patterns of the produced samples become broader. All samples exhibit a low degree of crystallinity, which implies that the graphene layers are randomly arranged along their stacking direction. Moreover, the peak of GO_2 can still be observed in the range of 2θ = 12.68–12.80°, denoting the coexistence of rGO and GO or the incompletion of the GO_2 reduction. Furthermore, as can be seen in Figure 3c, the diffraction reflections in the range of 2θ = 26.14–26.33° are attributed to the (002) plane. The determined values of $d_{(001)}$ are equal to 0.697 nm, 0.695 nm, and 0.691 nm, while the values of $d_{(002)}$ are 0.340 nm, 0.339 nm, and 0.338 nm, for rGO_2, rGO_2_5, and rGO_2_10, respectively. The smallest interlayer distance for the rGO_2_10 sample between all reduced products investigated in this research shows that the most efficient restoration of the π-conjugated system is obtained by using the GO_2 sample with the mixture of MA (10 wt%) and P_2O_5. Furthermore, XRD data showed that rGO samples derived from synthesized GO using the $H_2SO_4/H_3BO_3/CrO_3$ mixture exhibit lower *d*-spacing values compared to those of GO_1 reduced products. This tendency is probably related to the higher number of functional groups on the surface of GO_2 that during thermal treatment generates higher values of pressure and energy required for a more efficient reduction process of GO.

The behavior of the MA and P_2O_5 additive used to repair the π-conjugated system and defective sites of the graphene network during the annealing process were evaluated in detail by using Raman spectroscopy analysis. This technique was employed as a non-destructive, high-resolution, and fast tool to investigate the vibrational properties, the lattice structure, purity, defects, doping, and strain of carbon allotropes [39]. The Raman spectra of graphite, GO_1, GO_2, and thermally reduced GO_1 and GO_2 samples are shown in Figure 4.

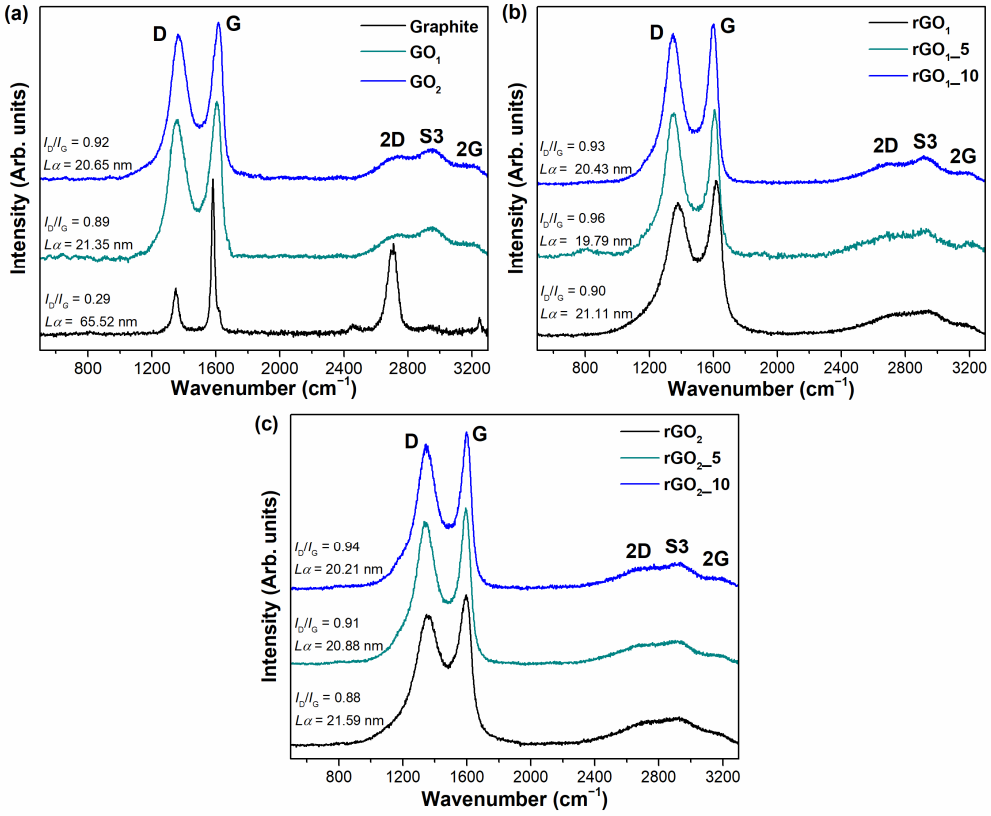

Figure 4. Raman spectra of graphite, GO_1, and GO_2 (**a**); thermally reduced samples derived from GO_1 (**b**); and thermally reduced samples derived from GO_2 (**c**). The excitation wavelength is 532 nm.

Figure 4 shows that recorded Raman spectra are similar between all synthesized samples. Each Raman spectrum consists of two dominant peaks located at ~1360 cm^{-1} and ~1600 cm^{-1}, corresponding to the D and G bands, which are typical modes of graphitic materials, respectively. The D band can be visualized as a breathing vibration of six-membered aromatic rings; defects and various disorders, such as carbon vacancies, grain boundaries, dislocations, sp^3 defects, armchair, or zigzag edges, are required for activation of this mode. The G band is associated with in-plane vibrations of pairs of sp^2 hybridized carbon atoms. This mode is always allowed in Raman spectra. The intensity ratio of the D and G modes (I_D/I_G) characterizes the degree of structural disorder in graphene-derived material. The number of defects decreases with a decrease in the I_D/I_G value [41–43]. Furthermore, the ratio of I_D/I_G could be used to determine an average crystallite size $L\alpha$ (Equation (4)) [28]. The second order bands are observed in the range of 2500–3300 cm^{-1}. The S3 peak located at ~2900 cm^{-1} is an overtone derived from the combination of D and G modes, while the 2G peak at ~3180 cm^{-1} is attributed to an overtone of the G band. The 2D band (also called the G′ band) at ~2700 cm^{-1} is a second-order band of the D peak. It is called the 2D band since it involves two of the same phonons responsible for the D band but it does not require the presence of the defects in the structure in contrast with the D band [44]. The value of I_{2D}/I_G (intensities ratio of 2D and G bands) defines the number of graphene layers in the structure. The number of layers increases with an increase of the G band intensity and the decrease of the 2D intensity [45]. In this study, the much higher intensity of the G peak is observed in all Raman spectra of synthesized samples compared to that of the 2D band. This suggests the multilayer structure in all obtained thermally reduced GO products.

As can be seen in Figure 4a, the ratio of I_D/I_G is found to be 0.89 and 0.92 for GO_1 and GO_2 samples, respectively. The higher I_D/I_G value for GO_2 indicates that this sample has a more defective structure than GO_1 due to the higher number of sp^3 defects and other disorders generated by the attachment of oxygen-containing functional groups to the graphene layers. Furthermore, the D and G bands in the GO_2 spectrum are shifted to higher

wavenumbers compared to that of GO_1, indicating a greater disruption of the conjugated structure after the oxidation process in the GO_2 sample. Meanwhile, Figure 4b,c indicates that the values of I_D/I_G for rGO samples obtained during thermal reduction of GO with MA and P_2O_5 additives varies from 0.91 to 0.96 and are slightly higher in comparison with those of pure GO. This increase might be due to the removal of functional groups and the high release of gaseous products during thermal reduction that causes disorders in the structure, such as vacancies, dislocations, armchair, and zigzag edges. Furthermore, from Figure 4b,c it can be noted that the thermal treatment of GO in the presence of additives causes a slightly higher I_D/I_G value than that of the thermal treatment of GO without additives. The value of the I_D/I_G could rise due to the presence of phosphorus atoms in the structure of the rGO samples, which were effectively introduced during thermal treatment of GO in the presence of the MA and P_2O_5 mixture. These phosphorus atoms could be attached to the graphene layer in the form of C–P–O or C–P=O bonds generating sp^3 defects and, also, may be able to replace carbon atoms creating new point defects in the structure due to the higher atomic radius of P than that of C atoms. Nonetheless, this slight increase of I_D/I_G does not detract from the benefits of the use of carbon suboxide in the thermal reduction of GO since lower values of I_D/I_G are obtained compared to the results investigated by other authors [18,29,45,46]. Furthermore, the values of $L\alpha$ vary from 19.79 to 21.59 nm between all synthesized samples showing that the crystallite size remains similar during the thermal treatment in the presence and absence of the addition of MA and P_2O_5 mixture.

The morphology of thermally reduced GO samples was studied using SEM analysis at 50,000× magnification (Figure 5). SEM images of the GO_1 and GO_2 samples (Figure 5a,e) present a well-ordered layered structure with folds and wrinkles. This is a consequence of the oxidative treatment of graphite by the attachment of oxygen functional groups. After thermal reduction of the pure GO_1 sample (Figure 5b), the layers agglomerate and form carbon derivatives of about 1 µm in size. The heat treatment of GO_1 with the mixture of MA (5 wt%) and P_2O_5 (Figure 5c) leads to irregular stacking of graphene layers with multiple folds. The further increase of additives in the thermal reduction of GO_1 creates a corrugated morphology, as can be seen in Figure 5d. These obtained folded sheets could be related not only to the reduction process but also to the insertion of phosphorus into the rGO_1_5 and rGO_1_10 structures, because the phosphorus atoms form a pyramid-like structure in the graphene sheet due to increased bond length and decreased bond angle [23,47]. After the reduction of pure GO_2 (Figure 5f), no agglomerates are observed, but the graphene layers are disrupted into smaller randomly arranged sheets. The rGO_2_10 sample is composed of numerous thin layers that are randomly stacked together, forming a porous network. Furthermore, as can be seen from Figure 5g,h, both reduced GO_2 samples in the presence of additives (rGO_2_5 and rGO_2_10) exhibit nanosheets with folded and crumpled features that could also be attributed to the doping of rGO with phosphorus atoms.

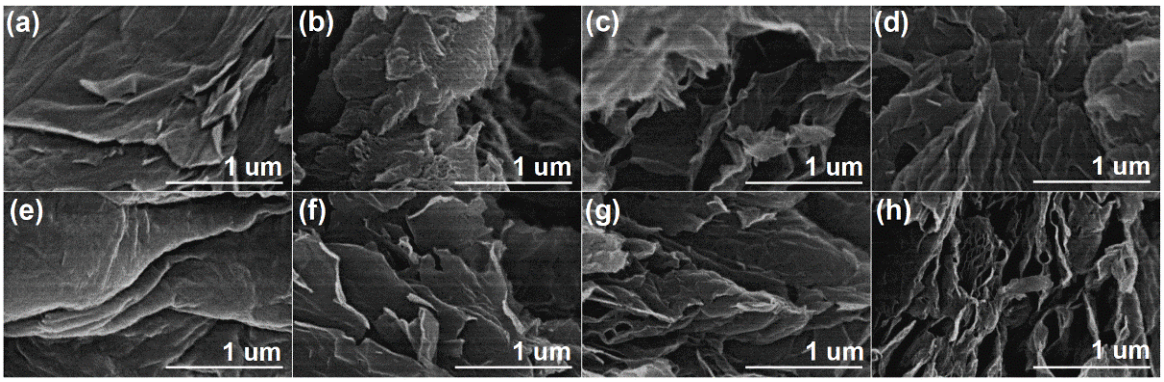

Figure 5. SEM images of GO_1 (**a**), rGO_1 (**b**), rGO_1_5 (**c**), rGO_1_10 (**d**), GO_2 (**e**), rGO_2 (**f**), rGO_2_5 (**g**), and rGO_2_10 (**h**) samples.

Electrical conductivity is one of the key characteristics determining the successful application of rGO in various electrochemical systems such as (bio)sensors, supercapacitors, fuel cells, etc. The electrical behavior of non-metallic powders, including carbonaceous compounds, could be estimated by monitoring the electrical conductivity of bulk materials under compression [48]. Consequently, in this study, the relationship between electrical conductivity (σ) on the logarithmic scale and bulk density (ρ_{bulk}) was determined. The results presented in Figure 6 reveal that the electrical conductivity of prepared carbon materials increases with the increasing of ρ_{bulk} value. This trend is in accordance with the electrical conductivity and resistivity results of graphene, graphite, graphite oxide, carbon black, and carbon nanotubes reported in [48–50]. By compressing a bulk material, closer contact between particles is achieved, leading to higher electrical conductivity because higher electron mobility is ensured in the sample. Following this, the highest electrical conductivity is established with maximum values of bulk density when the most compact arrangement of particles is obtained. The electrical conductivity of pristine graphite is dependent on the compression of the sample as well. From Figure 6a, it can be noted that graphite is a good electrical conductor. Log electrical conductivity varies in the range 1.47–3.53 S m^{-1}, approaching the theoretical values [50]. Besides, the maximum value of ρ_{bulk} for graphite powder is found to be 2.03 g cm^{-3}, which is a similar result to the theoretical value of its density reported in the literature (ρ = 2.26 g cm^{-3}) [51]. Meanwhile, the electrical conductivity of both synthesized GO_1 and GO_2 samples is significantly lower than that of graphite. This decrease is certainly due to the existence of a large number of oxygen-containing functional groups in the backbone of the graphene sheet. Upon oxidation treatment of graphite its band gap significantly broadens due to the disruption of the sp^2 carbon network and the attachment of numerous oxygen-containing functionalities to the surface that inhibit the effective electron transport. Furthermore, higher resistivity is estimated in the case of GO_2, which proves the higher degree of oxidation for GO_2 compared to that of GO_1.

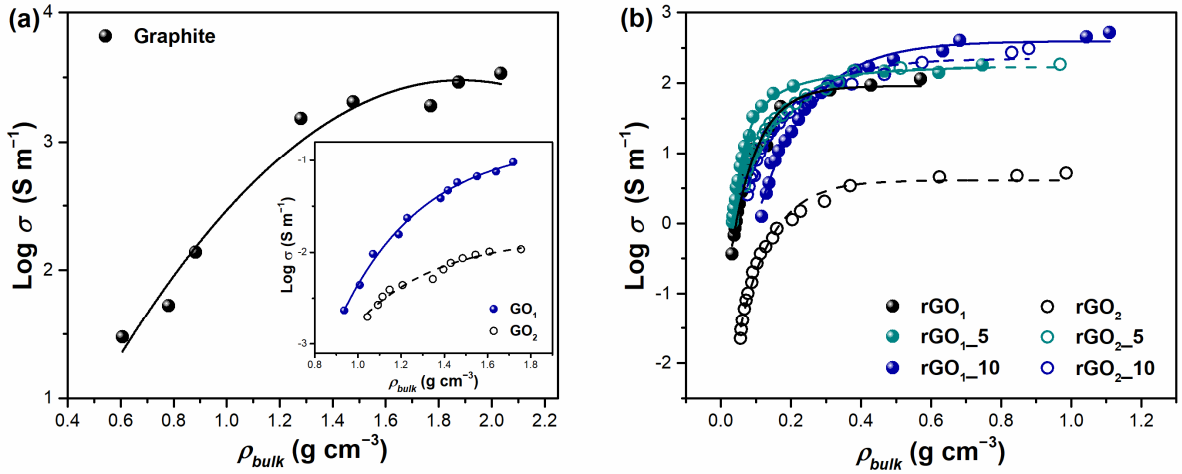

Figure 6. Electrical conductivity dependence on bulk density for graphite (**a**) and thermally reduced GO samples (**b**). The inset in (**a**) demonstrates the relationship between electrical conductivity and bulk density for GO_1 and GO_2 samples.

Figure 6b represents the dependence of electrical conductivity on bulk density for thermally reduced GO samples. It should be noted that the bulk density values for all annealed compounds are significantly decreased compared to those of their precursors (GO_1 and GO_2). This drastic change in density indicates the porous structure of products after thermal treatment. The highest bulk density corresponds to the rGO_1_10 sample (ρ_{bulk} = 1.11 g cm^{-3}), while the lowest density value is determined for the rGO_1 product (ρ_{bulk} = 0.57 cm^{-3}). Furthermore, a remarkable enhancement of electrical conductivity is observed after the thermal decomposition process of GO in the presence of the MA and

P_2O_5 mixture. The higher the amount of additives used in the thermal reduction reaction, the higher the conductivity achieved. In addition, higher electrical conductivity values in the case of rGO samples are achieved at lower densities than that of graphite. This makes these materials promising in the production of supercapacitor electrodes. Log conductivity (S m^{-1}) appears to be in the range of –0.43–2.05 for rGO_1, 0.01–2.25 for rGO_1_5, 0.09–2.72 for rGO_1_10, –1.65–0.71 for rGO_2, 0.53–2.26 for rGO_2_5, and 0.40–2.48 for rGO_2_10, showing the semi-conductor properties of samples. These electrical conductivity values of rGO are similar to previous reports found in the literature [49,52]. It should be highlighted that the most obvious advantage of the use of additives is observed in the set of thermally reduced GO_2 samples. As can be seen from Figure 6b, rGO_2 without additives shows the worst conductivity between all reduced products, but the addition of MA and P_2O_5 enhances electrical conductivity extremely in rGO_2_5 and rGO_2_10. These reduced samples exhibit values close to the reduced GO_1 products with additives indicating the achieved effective recovery of π-conjugated system. Moreover, it could be clearly seen that the addition of MA (10 wt%) and P_2O_5 in the thermal reduction of GO leads to the highest values of electrical conductivity between all reduced samples. This suggests that carbon suboxide used in the thermal reduction reaction of GO could repair the sp^2 hybridized carbon structure and improve electron mobility. However, the presence of phosphorus atoms observed by EDX and FTIR analysis could also influence the electrical behavior of the rGO_1_5, rGO_1_10, rGO_2_5, and rGO_2_10 samples because phosphorus atoms are capable of modulating the electronic structure and decreasing the resistivity of graphene-based derivatives. The incorporation of phosphorus species may increase the density of charge carries in the carbon product due to the contribution of phosphorus electrons to the graphene π-conjugated system [23]. Overall, the obtained electrical conductivity data indicate that the thermal reduction of GO with the use of the MA and P_2O_5 mixture has a positive impact on electronic properties of the final products. The relatively high conductivity at low values of bulk density demonstrates the possibility of applying thermally reduced GO samples for metal-free and cheap carbon-based electrode materials.

The samples having the highest values in electrical conductivity (rGO_1_10 and rGO_2_10) were analyzed using TEM analysis to compare their structure morphology and crystallinity in detail. Obtained TEM and SAED patterns are presented in Figure 7.

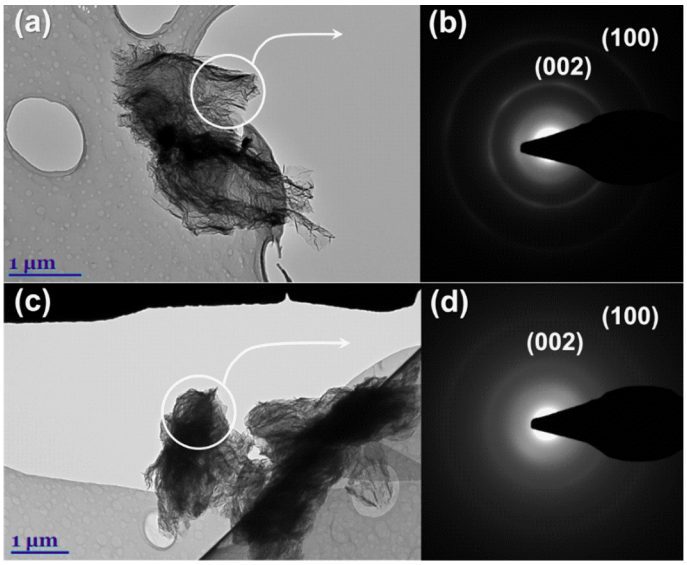

Figure 7. TEM images of—rGO_1_10 (**a**) and rGO_2_10 (**c**). SAED patterns of rGO_1_10 (**b**) and rGO_2_10 (**d**).

The TEM image of the rGO_1_10 specimen clearly shows several transparent reduced graphene oxide layers with wrinkled and folded features originated from the exfoliation process and incorporation of phosphorus atoms in the structure of graphene layer. However,

the existence of darker areas indicates thick stacking nanostructure in some regions. In contrast, rGO_2_10 consists of a remarkable multi-layered structure with corrugations that confirms the presence of structural defects in the nanosheets. The SAED images presented in Figure 7b,d show typical ring-like patterns indicating the polycrystalline nature of the rGO_1_10 and rGO_2_10 samples [53]. Nevertheless, the more obscure and featureless rings with unclear diffraction spots in the SAED image of rGO_2_10 are evidence of a more amorphous and disordered structure compared with that of rGO_1_10. For this reason, the rGO_2_10 sample may contain a larger number of sp^3 regions and phosphorus atoms in its structure. Based on obtained XRD analysis data it is determined that the inner ring shown in SAED images is associated with the diffraction of (002) planes and the outer ring describes (100) planes. This is in accordance with the study on the SAED patterns of reduced graphene oxide reported by Ngidi et al. [54]. The presence of both planes (002) and (100) confirms the partial restoration of sp^2 structure in both rGO_1_10 and rGO_2_10 samples.

4. Conclusions

In summary, we presented a novel and simple thermal reduction of a GO technique in the presence of malonic acid and phosphorus pentoxide that results in a repaired π-conjugated system and the incorporation of phosphorus atoms into the structure. It has been determined that structural and electrical properties or rGO samples depend on the amount of additive used and the type of GO. The best recovery of sp^2 hybridized carbon system was achieved using the mixture which has 10 wt% of malonic acid. Thermally reduced GO_1 samples in the presence of additives have higher values of electrical conductivity compared with those of annealed GO_2 samples. Furthermore, the investigation has showed the doping of phosphorus atoms in all rGO samples obtained using additives. The highest phosphorus content (2.3 at%) was achieved in rGO_2_10 compared to that of other samples synthesized. This suggests that samples prepared in this study could have a potential application in supercapacitors, biosensors, and fuel cells since the phosphorus-rich sites in rGO materials could act as electrochemical active regions, which can improve charge storage properties, increase charge carries, and enhance the capacity performance during electrochemical measurement. Moreover, the obtained findings set the direction for future research, suggesting that studies aimed at the full recovery of π-conjugated system and incorporation of high amounts of phosphorus-containing functionalities should focus on optimization of the GO-reduction process. It is still essential to test the effect of different temperatures, amount of additives, or pressure on the rGO structural changes.

Author Contributions: Conceptualization, J.B.; data curation, R.A.; funding acquisition, J.G.; investigation, R.A., G.N., M.S. and V.B.; methodology, J.B. and J.G.; supervision, J.B. and J.G.; visualization, R.A.; writing—original draft, R.A.; writing—review and editing, J.G., G.N., M.S., V.B. and J.B. All authors have read and agreed to the published version of the manuscript.

Funding: This research has received funding from European Social Fund (project No. 09.3.3-LMT-K-712-16-0154) under grant agreement with the Research Council of Lithuania (LMTLT).

Institutional Review Board Statement: Not applicable.

Informed Consent Statement: Not applicable.

Data Availability Statement: Data are contained within the article.

Conflicts of Interest: The authors declare no conflict of interest.

References

1. Ensafi, A.A.; Alinajafi, H.A.; Rezaei, B. Thermally reduced graphene oxide/polymelamine formaldehyde nanocomposite as a high specific capacitance electrochemical supercapacitor electrode. *J. Mater. Chem. A* **2018**, *6*, 6045–6053. [CrossRef]
2. Šakinyte, I.; Barkauskas, J.; Gaidukevič, J.; Razumiene, J. Thermally reduced graphene oxide: The study and use for reagentless amperometric d-fructose biosensors. *Talanta* **2015**, *144*, 1096–1103. [CrossRef]
3. Singh, R.K.; Kumar, R.; Singh, D.P. Graphene oxide: Strategies for synthesis, reduction and frontier applications. *RSC Adv.* **2016**, *6*, 64993–65011. [CrossRef]

4. Kurian, M. Recent progress in the chemical reduction of graphene oxide by green reductants–A Mini review. *Carbon Trends* **2021**, *5*, 100120. [CrossRef]
5. Barkauskas, J.; Gaidukevič, J.; Niaura, G. Thermal reduction of graphite oxide in the presence of nitrogen-containing dyes. *Carbon Lett.* **2021**, *31*, 1097–1110. [CrossRef]
6. Qiu, Y.; Collin, F.; Hurt, R.H.; Külaots, I. Thermochemistry and kinetics of graphite oxide exothermic decomposition for safety in large-scale storage and processing. *Carbon Lett.* **2021**, *31*, 1097–1110. [CrossRef]
7. Yang, G.; Li, L.; Lee, W.B.; Ng, M.C. Structure of graphene and its disorders: A review. *Sci. Technol. Adv. Mater.* **2018**, *19*, 613–648. [CrossRef]
8. Kaniyoor, A.; Baby, T.T.; Arockiadoss, T.; Rajalakshmi, N.; Ramaprabhu, S. Wrinkled graphenes: A study on the effects of synthesis parameters on exfoliation-reduction of graphite oxide. *J. Phys. Chem. C* **2011**, *115*, 17660–17669. [CrossRef]
9. Botas, C.; Álvarez, P.; Blanco, C.; Santamaría, R.; Granda, M.; Gutiérrez, M.D.; Rodríguez-Reinoso, F.; Menéndez, R. Critical temperatures in the synthesis of graphene-like materials by thermal exfoliation-reduction of graphite oxide. *Carbon* **2013**, *52*, 476–485. [CrossRef]
10. Zhang, P.; Li, Z.; Zhang, S.; Shao, G. Recent Advances in Effective Reduction of Graphene Oxide for Highly Improved Performance Toward Electrochemical Energy Storage. *Energy Environ. Mater.* **2018**, *1*, 5–12. [CrossRef]
11. Pei, S.; Cheng, H.M. The reduction of graphene oxide. *Carbon* **2012**, *50*, 3210–3228. [CrossRef]
12. Liang, Y.; Frisch, J.; Zhi, L.; Norouzi-Arasi, H.; Feng, X.; Rabe, J.P.; Koch, N.; Müllen, K. Transparent, highly conductive graphene electrodes from acetylene-assisted thermolysis of graphite oxide sheets and nanographene molecules. *Nanotechnology* **2009**, *20*, 434007. [CrossRef]
13. Bortolini, O.; Pandolfo, L.; Tomaselli, C.; Traldi, P. Ion-molecule chemistry of carbon suboxide in an ion-trap mass spectrometer. *Int. J. Mass Spectrom.* **1999**, *190–191*, 171–179. [CrossRef]
14. Allen, M. Carbon suboxide in Halley. *Nature* **1991**, *354*, 272. [CrossRef]
15. Palmer, H.; Cross, W. Carbon films from carbon suboxide decomposition. Inhibition by carbon monoxide and the heat of formation of C2O. *Carbon* **1966**, *3*, 475–481. [CrossRef]
16. Shao, M.; Wang, D.; Yu, G.; Hu, B.; Yu, W.; Qian, Y. The synthesis of carbon nanotubes at low temperature via carbon suboxide disproportionation. *Carbon* **2004**, *42*, 183–185. [CrossRef]
17. Aukstakojyte, R.; Gaidukevic, J.; Barkauskas, J. Thermal Reduction of Graphene Oxide in the Presence of Carbon Suboxide. *J. Solid State Chem.* **2021**, *301*, 122365. [CrossRef]
18. Li, R.; Wei, Z.; Gou, X.; Xu, W. Phosphorus-doped graphene nanosheets as efficient metal-free oxygen reduction electrocatalysts. *RSC Adv.* **2013**, *3*, 9978–9984. [CrossRef]
19. Niu, F.; Tao, L.-M.; Deng, Y.-C.; Wang, Q.-H.; Song, W.-G. Phosphorus doped graphene nanosheets for room temperature NH3 sensing. *New J. Chem.* **2014**, *38*, 2269–2272. [CrossRef]
20. Feng, L.; Qin, Z.; Huang, Y.; Peng, K.; Wang, F.; Yan, Y.; Chen, Y. Boron-, sulfur-, and phosphorus-doped graphene for environmental applications. *Sci. Total Environ.* **2019**, *698*, 134239. [CrossRef]
21. Poh, H.L.; Sofer, Z.; Nováček, M.; Pumera, M. Concurrent Phosphorus Doping and Reduction of Graphene Oxide. *Chem.—A Eur. J.* **2014**, *20*, 4284–4291. [CrossRef]
22. Hu, C.; Liu, D.; Xiao, Y.; Dai, L. Functionalization of graphene materials by heteroatom-doping for energy conversion and storage. *Prog. Nat. Sci.* **2018**, *28*, 121–132. [CrossRef]
23. Fan, X.; Xu, H.; Zuo, S.; Liang, Z.; Yang, S.; Chen, Y. Preparation and supercapacitive properties of phosphorus-doped reduced graphene oxide hydrogel. *Electrochim. Acta* **2019**, *330*, 135207. [CrossRef]
24. Kim, M.; Lee, J.; Jeon, Y.; Piao, Y. Phosphorus-doped graphene nanosheets anchored with cerium oxide nanocrystals as effective sulfur hosts for high performance lithium–sulfur batteries. *Nanoscale* **2019**, *11*, 13758–13766. [CrossRef]
25. Yan, X.; Chen, J.; Yang, J.; Xue, Q.; Miele, P. Fabrication of free-standing, electrochemically active, and biocompatible graphene oxide-polyaniline and graphene-polyaniline hybrid papers. *ACS Appl. Mater. Interfaces* **2010**, *2*, 2521–2529. [CrossRef]
26. Hummers, W.S., Jr.; Offeman, R.E. Preparation of Graphitic Oxide. *J. Am. Chem. Soc.* **1958**, *80*, 1339. [CrossRef]
27. Gaidukevic, J.; Aukstakojyte, R.; Navickas, T.; Pauliukaite, R.; Barkauskas, J. A novel approach to prepare highly oxidized graphene oxide: Structural and electrochemical investigations. *Appl. Surf. Sci.* **2021**, *567*, 150883. [CrossRef]
28. Cançado, L.G.; Takai, K.; Enoki, T.; Endo, M.; Kim, Y.A.; Mizusaki, H.; Jorio, A.; Coelho, L.N.; Magalhães-Paniago, R.; Pimenta, M.A. General equation for the determination of the crystallite size La of nanographite by Raman spectroscopy. *Appl. Phys. Lett.* **2006**, *88*, 163106. [CrossRef]
29. Zhang, C.; Mahmood, N.; Yin, H.; Liu, F.; Hou, Y. Synthesis of phosphorus-doped graphene and its multifunctional applications for oxygen reduction reaction and lithium ion batteries. *Adv. Mater.* **2013**, *25*, 4932–4937. [CrossRef]
30. MacIntosh, A.R.; Jiang, G.; Zamani, P.; Song, Z.; Riese, A.; Harris, K.J.; Fu, X.; Chen, Z.; Sun, X.; Goward, G.R. Phosphorus and Nitrogen Centers in Doped Graphene and Carbon Nanotubes Analyzed through Solid-State NMR. *J. Phys. Chem. C* **2018**, *122*, 6593–6601. [CrossRef]
31. Okotrub, A.; Kanygin, M.; Koroteev, V.; Stolyarova, S.; Gorodetskiy, D.; Fedoseeva, Y.; Asanov, I.; Bulusheva, L.; Vyalikh, A. Phosphorus incorporation into graphitic material via hot pressing of graphite oxide and triphenylphosphine. *Synth. Metals* **2019**, *248*, 53–58. [CrossRef]

32. Luceño-Sánchez, J.A.; Maties, G.; Gonzalez-Arellano, C.; Diez-Pascual, A.M. Synthesis and characterization of graphene oxide derivatives via functionalization reaction with hexamethylene diisocyanate. *Nanomaterials* **2018**, *8*, 870. [CrossRef] [PubMed]
33. Peng, W.; Li, H.; Hu, Y.; Liu, Y.; Song, S. Characterisation of reduced graphene oxides prepared from natural flaky, lump and amorphous graphites. *Mater. Res. Bull.* **2016**, *78*, 119–127. [CrossRef]
34. Ţucureanu, V.; Matei, A.; Avram, A.M. FTIR Spectroscopy for Carbon Family Study. *Crit. Rev. Anal. Chem.* **2016**, *46*, 502–520. [CrossRef]
35. Riahi, K.Z.; Sdiri, N.; Ennigrou, D.J.; Horchani-Naifer, K. Investigations on electrical conductivity and dielectric properties of graphene oxide nanosheets synthetized from modified Hummer's method. *J. Mol. Struct.* **2020**, *1216*, 128304. [CrossRef]
36. Verma, S.; Dutta, R.K. A facile method of synthesizing ammonia modified graphene oxide for efficient removal of uranyl ions from aqueous medium. *RSC Adv.* **2015**, *5*, 77192–77203. [CrossRef]
37. Zu, L.; Gao, X.; Lian, H.; Cai, X.; Li, C.; Zhong, Y.; Hao, Y.; Zhang, Y.; Gong, Z.; Liu, Y.; et al. High Electrochemical Performance Phosphorus-Oxide Modified Graphene Electrode for Redox Supercapacitors Prepared by One-Step Electrochemical Exfoliation. *Nanomaterials* **2018**, *8*, 417. [CrossRef]
38. Nie, L.; Wang, C.; Hou, R.; Li, X.; Sun, M.; Suo, J.; Wang, Z.; Cai, R.; Yin, B.; Fang, L.; et al. Preparation and characterization of dithiol-modified graphene oxide nanosheets reinforced alginate nanocomposite as bone scaffold. *SN Appl. Sci.* **2019**, *1*, 545. [CrossRef]
39. Sharma, N.; Sharma, V.; Vyas, R.; Kumari, M.; Kaushal, A.; Gupta, R.; Sharma, S.; Sachdev, K. A new sustainable green protocol for production of reduced graphene oxide and its gas sensing properties. *J. Sci. Adv. Mater. Devices* **2019**, *4*, 473–482. [CrossRef]
40. Gaidukevič, J.; Barkauskas, J.; Malaika, A.; Rechnia-Gorący, P.; Możdżyńska, A.; Jasulaitienė, V.; Kozłowski, M. Modified graphene-based materials as effective catalysts for transesterification of rapeseed oil to biodiesel fuel. *Chin. J. Catal.* **2018**, *39*, 1633–1645. [CrossRef]
41. Sengupta, I.; Chakraborty, S.; Talukdar, M.; Pal, S.K.; Chakraborty, S. Thermal reduction of graphene oxide: How temperature influences purity. *J. Mater. Res.* **2018**, *33*, 4113–4122. [CrossRef]
42. Stanford, V.L.; Vyazovkin, S. Thermal Decomposition Kinetics of Malonic Acid in the Condensed Phase. *Ind. Eng. Chem. Res.* **2017**, *56*, 7964–7970. [CrossRef]
43. Tuz Johra, F.; Lee, J.-W.; Jung, W.-G. Facile and safe graphene preparation on solution based platform. *J. Ind. Eng. Chem.* **2014**, *20*, 2883–2887. [CrossRef]
44. Ma, B.; Rodriguez, R.D.; Ruban, A.; Pavlov, S.; Sheremet, E. The correlation between electrical conductivity and second-order Raman modes of laser-reduced graphene oxide. *Phys. Chem. Chem. Phys.* **2019**, *21*, 10125–10134. [CrossRef] [PubMed]
45. Muzyka, R.; Drewniak, S.; Pustelny, T.; Chrubasik, M.; Gryglewicz, G. Characterization of graphite oxide and reduced graphene oxide obtained from different graphite precursors and oxidized by different methods using Raman spectroscopy. *Materials* **2018**, *11*, 1050. [CrossRef] [PubMed]
46. Kumar, R.; Kaur, A. Chemiresistive gas sensors based on thermally reduced graphene oxide for sensing sulphur dioxide at room temperature. *Diam. Relat. Mater.* **2020**, *109*, 108039. [CrossRef]
47. Wang, H.-M.; Chen, Y.; Liu, Y.-J.; Zhao, J.-X.; Cai, Q.-H.; Wang, X.-Z. Phosphorus-doped graphene and (8, 0) carbon nanotube: Structural, electronic, magnetic properties, and chemical reactivity. *Appl. Surf. Sci.* **2013**, *273*, 302–309. [CrossRef]
48. Marinho, B.; Ghislandi, M.; Tkalya, E.; Koning, C.E.; de With, G. Electrical conductivity of compacts of graphene, multi-wall carbon nanotubes, carbon black, and graphite powder. *Powder Technol.* **2012**, *221*, 351–358. [CrossRef]
49. Gaidukevič, J.; Pauliukaitė, R.; Niaura, G.; Matulaitienė, I.; Opuchovič, O.; Radzevič, A.; Astromskas, G.; Bukauskas, V.; Barkauskas, J. Synthesis of reduced graphene oxide with adjustable microstructure using regioselective reduction in the melt of boric acid: Relationship between structural properties and electrochemical performance. *Nanomaterials* **2018**, *8*, 889. [CrossRef]
50. Rattanaweeranon, S.; Limsuwan, P.; Thongpool, V.; Piriyawong, V.; Asanithi, P. Influence of Bulk Graphite Density on Electrical Conductivity. *Procedia Eng.* **2012**, *32*, 1100–1106. [CrossRef]
51. Ayyappadas, C.; Shanu, O.S.; Vijayan, A.; Mohammed, I.A.; Vishnu, V.; Shamnadh, M. Effect of graphene, SiC and graphite addition on hardness, microstructure and electrical conductivity of microwave sintered copper MMCs fabricated by powder metallurgy route. *J. Phy. Conf. Ser.* **2019**, *1355*, 012035. [CrossRef]
52. Park, H.; Lim, S.; Du Nguyen, D.; Suk, J.W. Electrical measurements of thermally reduced graphene oxide powders under pressure. *Nanomaterials* **2019**, *9*, 1387. [CrossRef] [PubMed]
53. Wilson, D.; Sheng, K.; Yang, W.; Jones, R.; Dunlap, N.; Read, P. Modern Electron Microscopy in Physical and Life Sciences: Electron Diffraction. 2016. Available online: https://www.intechopen.com/chapters/49537 (accessed on 28 August 2022).
54. Ngidi, N.P.D.; Ollengo, M.A.; Nyamori, V.O. Effect of Doping Temperatures and Nitrogen Precursors on the Physicochemical, Optical, and Electrical Conductivity Properties of Nitrogen-Doped Reduced Graphene Oxide. *Materials* **2019**, *12*, 3376. [CrossRef] [PubMed]